

Estimation of cerebral oxy- and deoxy-haemoglobin concentration changes in a layered adult head model using near-infrared spectroscopy and multivariate statistical analysis

Terence S Leung, Clare E Elwell and David T Delpy

Department of Medical Physics and Bioengineering, Malet Place Engineering Building,
University College London, Gower Street, London WC1E 6BT, UK

Received 5 May 2005, in final form 16 September 2005

Published 30 November 2005

Online at stacks.iop.org/PMB/50/5783

Abstract

The non-invasive measurement of cerebral oxy- ($\Delta\text{HbO}_2^{\text{br}}$) and deoxy-haemoglobin ($\Delta\text{HHb}^{\text{br}}$) changes using near-infrared spectroscopy instruments is often affected by the absorption in the extracerebral layer. We have exploited the multivariate calibration (partial least squares, PLS) method to minimize the errors for a range of blood volume, oxygen saturation and extracerebral layer thicknesses. The changes in the mean time of flight of photons ($\Delta\tau$) and attenuation (ΔA) on the surface of a 3D adult head model were simulated using a finite-element method based on the diffusion equation. The PLS was then performed to identify the optimal number of detectors, their positions and weightings, to optimize the estimation of $\Delta\text{HbO}_2^{\text{br}}$ and $\Delta\text{HHb}^{\text{br}}$. We define the ‘nominal accuracy’ as the accuracy of estimating $\Delta\text{HbO}_2^{\text{br}}$ and $\Delta\text{HHb}^{\text{br}}$ over a nominal range of extracerebral layer thicknesses and ‘robustness’ as the accuracy beyond the nominal range. The results showed that for one or two detectors, $\Delta\tau$ performed better than ΔA while using them together gave the best performance. When more detectors were used, the performances of using $\Delta\tau$, ΔA or both together became comparable, showing that a larger number of detectors can compensate for the performance of a simple ΔA measurement despite this measurement having a relatively lower sensitivity to intracerebral absorption changes.

1. Introduction

Near-infrared spectroscopy (NIRS) has been widely used in medical and physiological research for the non-invasive assessment of oxygenation of the human brain both in adults and infants. With continuous-wave systems, changes in oxy- and deoxy-haemoglobin (ΔHbO_2 and ΔHHb) can be calculated from the measured attenuation changes using a modified Beer–Lambert law

(Delpy and Cope 1997). Alternatively, using time-domain (Kienle and Patterson 1997), frequency-domain (Fantini *et al* 1994) or spatially resolved systems (Farrell *et al* 1992, Suzuki *et al* 1999) the absolute tissue absorption coefficient (μ_a) can be derived (usually using algorithms based on the diffusion equation and an assumed homogeneous medium). From this, absolute HbO₂ and HHb can be calculated.

The availability of Δ HbO₂ measurement has made it possible to measure cerebral blood flow and cerebral blood volume with Δ HbO₂ as the tracer (Edwards *et al* 1993, Elwell *et al* 1994, Leung *et al* 2003). With indocyanine green as the tracer, cerebral blood volume, cerebral blood flow and the total circulating blood volume can also be measured by a NIRS system with three or more wavelengths (Hopton *et al* 1999, Gora *et al* 2002, Leung *et al* 2004). The absolute values for these parameters are often lower than those reported using other techniques such as positron emission tomography or magnetic resonance imaging (MRI), and the discrepancy is usually attributed to the effect of the overlying extracerebral layers i.e., the skin and skull on the optical pathlength used in the calculation and/or the assumption that the tissue is homogeneous. In reality, the head is not homogeneous. The brain is enclosed in the skull which is overlaid by the skin, both of which are perfused with blood. Optical measurements obtained on the surface of a head therefore measure absorptions due to the skin, skull, cerebrospinal fluid and the brain. The effects of inhomogeneity on surface measurements have been discussed in the literature. Hunter *et al* used the time-domain system and the simple diffusion model to measure oxygen saturation (SO₂) in the bottom layer of a 2-layer muscle phantom and found errors of 5–11% depending on the thickness of the top layer and its optical properties (Hunter *et al* 2002). Okada *et al* used Monte Carlo simulation of an adult human head model and found that the sensitivity of the cerebral attenuation signals reduced as the thickness of the upper layer increased (Okada and Delpy 2003a).

Analytical solutions to the diffusion equation have also been derived for simple layered models and it has been found that the μ_a of the lower layer can be measured most accurately when the thickness of the upper layer is known (Dayan *et al* 1992, Kienle *et al* 1998, Kienle and Glanzmann 1999). The idea of the partial differential pathlength (PDP) has also been developed to account for the mean pathlength in each tissue layer (Hiraoka *et al* 1993) while its time-domain counterpart, namely the mean time sensitivity factor (MTSF), provides a sensitivity measure for the mean time of flight to a small change in absorption in different layers (Steinbrink *et al* 2001). A recent paper (Fabbri *et al* 2004) compared three methods of measuring $\Delta\mu_a$ in the lower layer, namely, (a) the multidistance, frequency-domain method based on the diffusion theory, (b) the modified Beer–Lambert law based on a single distance method and (c) the modified Beer–Lambert law based on a two distance method. They concluded that method (c) performed best in estimating $\Delta\mu_a$ in the lower layer for upper layer thicknesses of 0.8 or 1.4 cm. However, to use method (c), the PDPs need to be estimated by the computationally intensive Monte Carlo simulation. A multidistance time-domain system has been developed recently to measure intracerebral and extracerebral changes in absorption with moments of the distributions of times of flight of photons following an injection of indocyanine green (Liebert *et al* 2004, 2005). The study showed that a delay in bolus transit time between two hemispheres can be identified in patients with cerebral perfusion deficit. Apart from using multiple detectors, it has also been suggested that a single distance, time-domain method can be used to measure μ_a in the upper and lower compartments in a three-layered phantom, given the depth of the three compartments is known (Steinbrink *et al* 2001).

To accurately measure μ_a of the brain (and hence HbO₂ and HHb), most of these techniques require the thickness of the extracerebral layer to be known which can be measured from CT, MRI or ultrasound scans. However, in the absence of any structural information, we need to know the error magnitude caused by assuming default values for the thickness of

Table 1. Summary of modelled parameter variations: ΔHbT in different layers is calculated by subtracting the reference values of HbT (see the end of section 3.1) at different layers from the HbT in the range, e.g. ΔHbT at layer 1 = $(30:10:70) - 50 = (-20:10:20)$.

Layer	Parameters	Range (min:step:max)
Extracerebral layer: skin/skull (layer 1)	Blood volume,	
	HbT (μM)	30:10:70
	ΔHbT (μM)	-20:10:20
	Oxygen saturation, SO_2 (%)	0.5:0.1:0.9
	Transport scattering coefficient, μ'_s (mm^{-1})	1.8
Intracerebral layer: grey matter (layer 2)	Blood volume,	
	HbT (μM)	60:10:100
	ΔHbT (μM)	-20:10:20
	Oxygen saturation, SO_2 (fraction)	0.5:0.1:0.9
	Transport scattering coefficient, μ'_s (mm^{-1})	2.2
Intracerebral layer: white matter (layer 3)	HbT (μM)	40
	ΔHbT (μM)	0
	Oxygen saturation, SO_2 (fraction)	0.7
	Transport scattering coefficient, μ'_s (mm^{-1})	9.1

the extracerebral layer while the real thickness, blood volume and oxygen saturation (SO_2) in different layers vary. The aim of this study was to investigate these errors and their minimization using multiple detectors at optimal locations measuring both intensity and mean time of flight.

In this paper, we mainly focus on the accuracy of measuring ΔHbO_2 and ΔHHb in the brain (denoted by $\Delta\text{HbO}_2^{\text{br}}$ and $\Delta\text{HHb}^{\text{br}}$) over a range of blood volume, SO_2 and thicknesses of different layers. The frameworks of PDPs and MTSFs have been adopted which are linear and suitable for multivariate calibration. We used light transport simulation software developed at UCL (Arridge *et al* 1993) to generate intensity and mean time of flight data at different source–detector spacings on a three-layered adult head model representing skin/skull, the grey matter and the white matter. A range of data were simulated (table 1) corresponding to different thicknesses and physiological conditions of each layer and these were used to produce calibrations for $\Delta\text{HbO}_2^{\text{br}}$ and $\Delta\text{HHb}^{\text{br}}$ using partial least squares. We have investigated the optimal number of detectors to use, the measurements made (attenuation or mean time of flight) their positions and the relative weightings to optimize the estimation of $\Delta\text{HbO}_2^{\text{br}}$ and $\Delta\text{HHb}^{\text{br}}$.

2. Theory

We first briefly review the concepts of PDP and MTSF and subsequently form our basic calibration models under this framework. We then discuss the optimization of estimating $\Delta\text{HbO}_2^{\text{br}}$ and $\Delta\text{HHb}^{\text{br}}$ over a range of thicknesses, blood volumes and SO_2 using the multivariate calibration technique of partial least squares.

2.1. Calibration models based on the partial differential pathlength and the mean time sensitivity factor

The PDP concept was introduced (Hiraoka *et al* 1993) to extend the modified Beer–Lambert law to heterogeneous media. The PDP at layer n , i.e. PDP_n is defined as a partial derivative of the measured attenuation A versus the absorption coefficient μ_a of each layer, i.e. $\text{PDP}_n = \frac{\partial A}{\partial \mu_{an}}$

where $n = 1, \dots, N$ and N is the number of layers. Note that A is defined here with base of e to match that of μ_s . To a first approximation, the partial derivative can be linearized, i.e. $\text{PDP}_n = \Delta A / \Delta \mu_{an}$ which is reasonable when $\Delta \mu_{an}$ is small, i.e. $\sum_n |\text{PDP}_n \Delta \mu_{an}| \ll 1$ (Steinbrink *et al* 2001, Liebert *et al* 2004). The PDP_n can also be considered as the mean pathlength of the light in layer n . In general, for a measurement configuration with one source and M detectors at different spacings, the total attenuation change from a heterogeneous medium at detector m can be expressed as

$$\Delta A_m = \sum_{n=1}^N \text{PDP}_{m,n} \Delta \mu_{an} \quad (1)$$

where $\text{PDP}_{m,n}$ corresponds to layer n within the field of view of detector m . The MTSF is the time-domain counterpart of the PDP. It is widely used in time-domain systems (Steinbrink *et al* 2001, Kohl-Bareis *et al* 2002, Liebert *et al* 2004, 2005) to calculate $\Delta \mu_a$ from changes in the mean time of flight ($\Delta \tau$):

$$\Delta \tau_m = \sum_{n=1}^N \text{MTSF}_{m,n} \Delta \mu_{an} \quad (2)$$

where $\text{MTSF}_{m,n}$ corresponds to the sensitivity of τ in response to a small change in μ_a in layer n within the field of view of detector m , i.e. $\text{MTSF}_{m,n} = \partial \tau_m / \partial \mu_{an}$ and can be calculated from a function of the PDP and τ at different layers.

In this paper, we mainly focus on changes in absorption in two of the layers, i.e. the skin/skull ($\Delta \mu_a^{\text{sk}}$) and the brain ($\Delta \mu_a^{\text{br}}$) and thus $N = 2$ here. Although the brain layer is subdivided into the grey matter and the white matter later in the paper where surface measurements of intensity and mean time of flight are simulated, we only introduce a change of absorption in the grey matter but not the white matter. In matrix form, $\Delta \mu_a^{\text{sk}}$ and $\Delta \mu_a^{\text{br}}$ (i.e. $\Delta \mu_{a1}$ and $\Delta \mu_{a2}$) can be calculated by

$$\boldsymbol{\mu} = \mathbf{L}^{-1} \mathbf{X} \quad (3)$$

where

$$\boldsymbol{\mu} = \begin{bmatrix} \Delta \mu_a^{\text{sk}} \\ \Delta \mu_a^{\text{br}} \end{bmatrix} \quad \mathbf{L} = \begin{bmatrix} J_1^{\text{sk}} & J_1^{\text{br}} \\ \vdots & \vdots \\ J_M^{\text{sk}} & J_M^{\text{br}} \end{bmatrix} \quad \mathbf{X} = \begin{bmatrix} \Delta A_1 \\ \Delta A_2 \\ \vdots \\ \Delta A_M \end{bmatrix} \quad \text{or} = \begin{bmatrix} \Delta \tau_1 \\ \Delta \tau_2 \\ \vdots \\ \Delta \tau_M \end{bmatrix}$$

and \mathbf{L}^{-1} is the inverse of \mathbf{L} . We use the symbol J_M^{br} to denote either PDP or MTSF in a particular layer (brain or skin/skull) measured with detector M . When $M = N$, equation (3) has a unique solution. When $M > N$, there are more than one solution and \mathbf{L}^{-1} becomes the pseudo-inverse of \mathbf{L} which can be found by the least-square approach. Equation (3) shows that theoretically when PDPs/MTSFs are known for the two layers and the number of detectors is larger than or equal to the number of layers ($M \geq N = 2$), $\Delta \mu_a^{\text{br}}$ (and $\Delta \mu_a^{\text{sk}}$) can be calculated from surface measurements ΔA_m or $\Delta \tau_m$. Unfortunately, both the PDP and MTSF cannot be measured but can be estimated by Monte Carlo simulations (Okada and Delpy 2003a, Steinbrink *et al* 2001).

The oxy- and deoxy-haemoglobin concentration changes in the brain, i.e. $\Delta \text{HbO}_2^{\text{br}}$ and $\Delta \text{HHb}^{\text{br}}$ can be calculated from $\Delta \mu_a^{\text{br}}$ measured at two (or more) wavelengths, usually at either side of the isobestic point (800 nm), using the Lambert law, i.e. $\boldsymbol{\mu} = \boldsymbol{\varepsilon} \mathbf{C}$ where $\boldsymbol{\varepsilon}$ is the specific absorption coefficient (log base e) and $\mathbf{C} = [\Delta \text{HHb}^{\text{br}} \Delta \text{HbO}_2^{\text{br}}]^T$. In this paper, we only discuss two wavelength measurements but the same principle can be extended to more wavelengths. It follows that $\mathbf{C} = \boldsymbol{\varepsilon}^{-1} \boldsymbol{\mu}$ where

$$\boldsymbol{\varepsilon}^{-1} = \begin{bmatrix} \varepsilon_{\text{HHb}}(\lambda_1) & \varepsilon_{\text{HbO}_2}(\lambda_1) \\ \varepsilon_{\text{HHb}}(\lambda_2) & \varepsilon_{\text{HbO}_2}(\lambda_2) \end{bmatrix}^{-1} = \begin{bmatrix} k_{11} & k_{12} \\ k_{21} & k_{22} \end{bmatrix} \quad (4)$$

and k_{ij} is the element of the inverse of the matrix containing the specific absorption coefficients of HbO₂ and HHb. Subsequently, $\Delta\text{HbO}_2^{\text{br}}$ and similarly $\Delta\text{HHb}^{\text{br}}$ can be written as

$$\begin{aligned} \Delta\text{HHb}^{\text{br}} &= k_{11}\Delta\mu_a^{\text{br}}(\lambda_1) + k_{12}\Delta\mu_a^{\text{br}}(\lambda_2) \\ \Delta\text{HbO}_2^{\text{br}} &= k_{21}\Delta\mu_a^{\text{br}}(\lambda_1) + k_{22}\Delta\mu_a^{\text{br}}(\lambda_2) \end{aligned} \tag{5}$$

or substituting equation (3) into (5),

$$\begin{aligned} \Delta\text{HHb}^{\text{br}} &= \sum_{m=1}^M [k_{11}w_{\text{HHb},m}(\lambda_1)\Delta X_m(\lambda_1) + k_{12}w_{\text{HHb},m}(\lambda_2)\Delta X_m(\lambda_2)] \\ \Delta\text{HbO}_2^{\text{br}} &= \sum_{m=1}^M [k_{21}w_{\text{HbO}_2,m}(\lambda_1)\Delta X_m(\lambda_1) + k_{22}w_{\text{HbO}_2,m}(\lambda_2)\Delta X_m(\lambda_2)] \end{aligned} \tag{6}$$

where $w_m(\lambda)$ is defined as the measurement weightings which are derived from \mathbf{L}^{-1} in equation (3) and are thus a function of PDPs/MTSFs and dependent upon layers' thicknesses and optical properties. Equations (1)–(6) are, however, only true if photon transport follows strictly the linear formulation suggested by equations (1) and (2). Photon transport in the head is actually a nonlinear process requiring modelling by more sophisticated methods (see section 3.1), therefore, we can only consider equation (3) as an approximation of a more complicated model.

2.2. Optimizing the estimation of $\Delta\text{HbO}_2^{\text{br}}$ and $\Delta\text{HHb}^{\text{br}}$ using the partial least squares

To optimize the estimation of $\Delta\text{HbO}_2^{\text{br}}$ and $\Delta\text{HHb}^{\text{br}}$ for a range of blood volume, SO₂ and thicknesses, we can no longer express $\Delta\mu_a^{\text{br}}$ generally in terms of PDPs/MTSFs and $\Delta A_m/\Delta\tau_m$ as in equations (1)–(3) because different blood volume, SO₂ and thicknesses result in different PDPs/MTSFs. Rather we use the notion of measurement weightings, $w_m(\lambda)$ which serve to weight surface measurements, ΔX_m of detector m in order to optimize the estimation of $\Delta\text{HbO}_2^{\text{br}}$, i.e.

$$\Delta\mu_a^{\text{br}}(\lambda) = \sum_{m=1}^M w_m(\lambda)\Delta X_m(\lambda) \tag{7}$$

where $\Delta X_m = \Delta A_m$ and/or $\Delta\tau_m$. Substituting (7) into (5) yields an expression similar to equation (6) but $w_{\text{HHb},m}(\lambda)$ and $w_{\text{HbO}_2,m}(\lambda)$ are now measurement weightings which are not directly related to \mathbf{L}^{-1} . To find the optimal $w_{\text{HHb},m}(\lambda)$ and $w_{\text{HbO}_2,m}(\lambda)$ for a range of physiological conditions (specifically corresponding to blood volume and SO₂ in different layers) and thicknesses (corresponding to differences in anatomy), we have carried out multivariate calibration on a set of simulated ΔA_m and/or $\Delta\tau_m$ with known $\Delta\text{HbO}_2^{\text{br}}$ and $\Delta\text{HHb}^{\text{br}}$. The formulation can be written in a form suitable for multivariate calibration, i.e.

$$\mathbf{y} = \mathbf{X}\mathbf{w} \tag{8}$$

where

$$\begin{aligned} \mathbf{X} &= \begin{bmatrix} k_{21}\Delta X_1(\lambda_1, t_1) & \cdots & k_{21}\Delta X_M(\lambda_1, t_1) & k_{22}\Delta X_1(\lambda_2, t_1) & \cdots & k_{22}\Delta X_M(\lambda_2, t_1) \\ \vdots & & \vdots & \vdots & & \vdots \\ k_{21}\Delta X_1(\lambda_1, t_P) & \cdots & k_{21}\Delta X_M(\lambda_1, t_P) & k_{22}\Delta X_1(\lambda_2, t_P) & \cdots & k_{22}\Delta X_M(\lambda_2, t_P) \end{bmatrix} \\ \mathbf{y} &= \begin{bmatrix} \Delta\text{HbO}_2^{\text{br}}(t_1) \\ \vdots \\ \Delta\text{HbO}_2^{\text{br}}(t_P) \end{bmatrix} \\ \mathbf{w}^T &= [\mathbf{w}_{\lambda_1} \quad \mathbf{w}_{\lambda_2}] = [w_{\text{HbO}_2,1}(\lambda_1) \quad \cdots \quad w_{\text{HbO}_2,M}(\lambda_1) \quad w_{\text{HbO}_2,1}(\lambda_2) \quad \cdots \quad w_{\text{HbO}_2,M}(\lambda_2)] \end{aligned}$$

and \mathbf{y} is the target, \mathbf{X} a set of measurements and \mathbf{w} the optimal measurement weightings. (In the multivariate calibration literature, the measurement weightings are often referred to as regression coefficients.) In our case, \mathbf{y} is $\Delta\text{HbO}_2^{\text{br}}$ and \mathbf{X} is a set of surface measurements, $\Delta X_m(\lambda)$ from M detectors at two wavelengths. Each row of \mathbf{X} contains the product of k (refer to equation (4)) and simulated surface measurement $\Delta X_m(\lambda)$ at detector m resulting from the p th physiological condition (signified by t_p), while each row of \mathbf{y} contains the corresponding $\Delta\text{HbO}_2^{\text{br}}$ in the p th physiological condition. Equation (8) is also applicable for estimating $\Delta\text{HHb}^{\text{br}}$ in which case one needs to replace $\Delta\text{HbO}_2^{\text{br}}$ with $\Delta\text{HHb}^{\text{br}}$ in \mathbf{y} , $w_{\text{HbO}_2,m}$ with $w_{\text{HHb},m}$ in \mathbf{w} and k_{21}/k_{22} with k_{11}/k_{12} in \mathbf{X} .

Equation (8) is a classical formulation in multivariate calibration and the literature in this field is abundant. The aim is to find the regression vector \mathbf{w} (termed as measurement weightings here) using a collection of measurement \mathbf{X} and known values \mathbf{y} . There are a number of ways to perform the calibration, including multiple linear regression, principal component regression and partial least squares (Martens and Naes 1991). We mainly consider the use of partial least squares (PLS) because it has better performance than other techniques in terms of handling collinearity and prediction. In PLS, the optimal weighting \mathbf{w} can be considered as a projection of the original measurements onto a new plane with a given number of principal components which captures the largest amount of variance in \mathbf{X} and at the same time optimizes the correlation between \mathbf{X} and \mathbf{y} . The PLS calibration has been implemented with a version known as SIMPLS for its speed and efficiency (de Jong 1993).

3. Methods

3.1. Light transport modelling

The simulated surface measurements ΔA_m and $\Delta\tau_m$ in this paper were generated with a software known as time-resolved optical absorption and scattering tomography (TOAST) developed at UCL (Arridge *et al* 1993). It is based on solving the diffusion equation with the finite-element method and provides fast computation which is crucial in this study because of the need to generate thousands of datasets. The adult head has been modelled as a three-dimensional spherical slab with three layers corresponding to the skin/skull (extracerebral layer), grey matter and white matter. Five 3D meshes corresponding to five different extracerebral layer thicknesses were generated using the automatic mesh generator NETGEN (Schoberl 2001). The radius of curvature of the superficial layer was set to 90 mm. Because of signal-to-noise ratio considerations, most NIRS instruments are typically limited to measuring out to an optode spacing of about 50 mm (assuming a 1 Hz sampling rate) (Evans 1997, Harris *et al* 1994) and this limitation has been included in the model. The dimension of the mesh, and the locations of the source and ten detectors are shown in figure 1. The first detector is 5 mm from the source and subsequent detectors are 5 mm apart.

A wide range of absorption coefficients for each layer were simulated, based upon physiologically reasonable values for parameters such as the total haemoglobin concentration (HbT, in μM , representing blood volume), haemoglobin oxygen saturation (SO_2 , expressed as a fraction), water content (W , in fraction), background absorption (B , in mm^{-1}). The variations in parameters are summarized in table 1. The absorption coefficient of each layer is calculated as follows:

$$\mu_a(\lambda) = \varepsilon_{\text{HHb}}(\lambda)\text{HbT}(1 - \text{SO}_2) + \varepsilon_{\text{HbO}_2}(\lambda)\text{HbT} \cdot \text{SO}_2 + \mu_{a,\text{H}_2\text{O}}(\lambda)W + B \quad (9)$$

where $\mu_{a,\text{H}_2\text{O}}(\lambda)$ is the absorption coefficient of 100% water and B is a wavelength independent background absorption. The transport scattering coefficients (μ'_s) are set as 1.8, 2.2 and

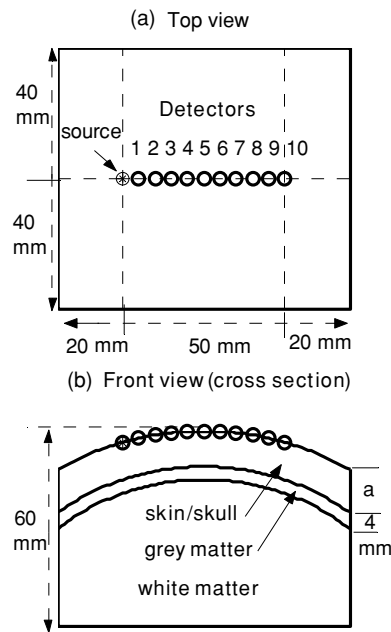


Figure 1. An adult head has been modelled by 3D spherical slabs: (a) the top view shows the locations of the source and the ten detectors; the top surface is spherically bounded by rectangular boundaries; (b) the front view (cross section). The thickness of the skin/skull is denoted by a which is varied between 7, 9, 11, 13 and 15 mm. The radius of curvature of the superficial layer was set to 90 mm.

9.1 mm^{-1} ($\lambda = 780 \text{ nm}$) for the skin/skull, grey matter and white matter, respectively and are the same as those in Okada and Delpy (2003a). The tissue water contents of the grey and white matters are set to 80% (by volume) which is the value considered in Matcher and Cooper (1994) and Hueber *et al* (2001). The skin/skull generally contains less water and an estimate of 70% is used here. Previous studies showed evidence of the existence of a wavelength-independent background absorption in the head accounting for absorbers other than HbO_2 , Hb and water (Essenpreis *et al* 1993). The background absorption B is fixed at 0.003 mm^{-1} (at all wavelengths) for all layers so that the overall μ_a in each layer match the range of those given in Okada and Delpy (2003a). The wavelength dependency of μ'_s is also taken into account based on a previous study (Matcher *et al* 1997) which showed that experimentally measured μ'_s decreases approximately linearly with wavelength in the human head, for example, when $\mu'_s(780 \text{ nm})$ is 1 mm^{-1} , $\mu'_s(820 \text{ nm})$ is scaled to 0.9534 mm^{-1} .

As shown in table 1, the values of four variables were changed one by one over five steps between the minimum and maximum values in the range making a total of $625 (= 5^4)$ sets of data. Each dataset contained estimates of intensity and mean time of flight at the ten detector positions shown in figure 1 and for two wavelengths (780 and 820 nm). The intensity measurements (I) were converted to change in attenuations by the conventional formulation: $\Delta A = -\log_e(I/I_0)$ where I_0 is the reference intensity and generated by the head model in which HbT in the skin/skull = $50 \mu\text{M}$, HbT in the grey matter = $80 \mu\text{M}$, HbT in the white matter = $40 \mu\text{M}$ and SO_2 in all layers = 0.7. The change in the mean time of flight $\Delta\tau$ was also calculated with respect to τ_0 generated with the same reference values. A previous study reported mean values of 5.2% and 2.7% for blood volumes in the grey and

white matters, respectively (Leenders *et al* 1990). These values were converted to HbT in μM as specified above using the conversion equation given in Wyatt *et al* (1990) with a nominal venous haemoglobin concentration of 14 g dl^{-1} . The skin/skull normally has a μ_a slightly smaller than that of the grey matter but larger than that of the white matter. Subsequently, an estimate of HbT of $50 \mu\text{M}$ is given for the skin/skull blood volume.

3.2. Performing partial least squares calibration

In the absence of any structural information such as MRI/CT/ultrasound scans, the thicknesses of the different layers are not known. Under this circumstance, one may adopt a methodology which assumes certain thicknesses, blood volume and SO_2 for each layer when in fact they are variable. We investigated such errors that would arise through the calculation of $\Delta\text{HbO}_2^{\text{br}}$ and $\Delta\text{HHb}^{\text{br}}$ based on the simulated ΔA_m and $\Delta\tau_m$ measurements at multiple detectors. Known $\Delta\text{HbO}_2^{\text{br}}$ and $\Delta\text{HHb}^{\text{br}}$ were calibrated against simulated ΔA_m and/or $\Delta\tau_m$ for extracerebral layer thicknesses of 9, 11 and 13 mm, and blood volume and SO_2 values as described in table 1. The PLS calibration was performed with a predefined number of principal components (see section 4.1). The calibration resulted in the measurement weightings $w_{\text{HbO}_2, m}$ and $w_{\text{HHb}, m}$ described in equation (6) which optimized the estimation of $\Delta\text{HbO}_2^{\text{br}}$ and $\Delta\text{HHb}^{\text{br}}$ respectively. The calibrated model was then tested with a wider range of extracerebral layer thicknesses of 7, 9, 11, 13 and 15 mm. There are a total of 1875 values of $\Delta\text{HbO}_2^{\text{br}}/\Delta\text{HHb}^{\text{br}}$ in the training dataset and 3125 values in the testing dataset.

One aim of this work is to find the optimal combination of detectors and measurement types from a set of K detectors placed along a straight line. For example, if three detectors are to be chosen out of the ten detectors as shown in figure 1. The possible combinations can include: detectors 1, 2, 3; detectors 1, 2, 4; detectors 1, 2, 5 and so on. The total possible number of combinations is given by the binomial coefficient ${}_K C_M = K!/[M!(K-M)!]$ in which M elements are selected from a total of K elements, and in this example is 120. To find the optimal combinations of detectors for a total of M detectors, we have performed PLS calibrations on all possible combinations of detectors and worked out the root-mean-square (RMS) errors between the predicted and real $\Delta\text{HbO}_2^{\text{br}}$ and those of $\Delta\text{HHb}^{\text{br}}$ for each possible combination. For the cross-validation, the whole dataset was randomly split into five blocks of subsets, each containing 125 datasets. A calibration was performed using four blocks of subsets (500 datasets), while the remaining one (125 datasets) used for validation. Another four calibrations were carried out similarly using a different block of subsets for validation every time. This whole procedure was repeated five times after which the overall RMS error was calculated. There were altogether 25 calibrations and validations for each combination of detectors. In the above example whereby three detectors are to be selected from ten, the total number of calibrations and validations for all possible combinations of detectors becomes 3000 ($\equiv 120 \times 25$). (In comparison, the alternative leave-one-out validation technique requires the number of calibrations and validations equivalent to the total number of datasets for each combination of detectors, i.e. 625. The total number of calibrations and validations would therefore be 75 000 ($\equiv 120 \times 625$) which requires a considerably longer computation time with only marginally improved performance.) The average of the RMS errors for $\Delta\text{HbO}_2^{\text{br}}$ and $\Delta\text{HHb}^{\text{br}}$ has been used to assess the performance. We consider $\Delta\text{HbO}_2^{\text{br}}$ and $\Delta\text{HHb}^{\text{br}}$ together, rather than individually so that the optimal locations of detectors are applicable for the simultaneous estimation of both $\Delta\text{HbO}_2^{\text{br}}$ and $\Delta\text{HHb}^{\text{br}}$. The combination of detectors which results in the smallest RMS error is considered to be the optimal one. Analyses were carried out based on $K = 10$ and $M = 1, 2, 3, 6$ and 10 .

Table 2. Optimal combinations of detectors and the number of principal components used {curly brackets}: (i) the measurement data, i.e. $\Delta X_m = \Delta A_m$; (ii) $\Delta X_m = \Delta \tau_m$; (iii) $\Delta X_m = [\Delta A_m \times \text{scaling factor 1}, \Delta \tau_m \times \text{scaling factor 2}]$. Extracerebral thicknesses of 9, 11 and 13 mm were used in the calibration.

No. of detectors (M)	Optimal combinations of detectors (no. of principal components)		
	(i) ΔA	(ii) $\Delta \tau$	(iii) ΔA & $\Delta \tau$
1	10 {1}	10 {1}	10 {2}
2	1, 10 {3}	2, 9 {3}	2, 10 {6}
3	8, 9, 10 {4}	1, 4, 10 {4}	1, 8, 10 {8}
6	5, 6, 7, 8, 9, 10 {6}	1, 2, 4, 8, 9, 10 {6}	1, 2, 7, 8, 9, 10 {12}
10	1–10 {6}	1–10 {6}	1–10 {12}

3.3. Nominal accuracy and robustness

Optimal solutions (i.e., the number of principal components and locations of detectors) have been obtained using blocks of subsets of randomized training datasets and it is necessary to know how well the PLS calibration performs in datasets which have not been used during the training phase. In particular, we would like to know how robustly the measurement weightings, which are based on the extracerebral layer thicknesses of a nominal range, say 9, 11 and 13 mm, perform in situations when the extracerebral layer thicknesses vary over a wider range, say 7, 9, 11, 13 and 15 mm.

Two test datasets have been simulated, dataset (A): ΔA_m and $\Delta \tau_m$ from the extracerebral layer thicknesses of 9, 11 and 13 mm (nominal), and the range of blood volume and SO_2 as shown in table 1; and dataset (B): ΔA_m and $\Delta \tau_m$ from the extracerebral layer thicknesses of 7, 9, 11, 13 and 15 mm (nominal + extremes), and the range of blood volume and SO_2 as shown in table 1.

Before discussing the use of the two datasets mentioned above, we first describe an error term suitable for performance assessment. The errors (differences) between the real and predicted $\Delta HbO_2^{br} / \Delta HHb^{br}$ will vary for different real $\Delta HbO_2^{br} / \Delta HHb^{br}$. For instance, the errors between the predicted and real ΔHbO_2^{br} which result from a calibration based on three detectors as shown in table 2(ii) (to be discussed in more details in section 4.1) are given in figure 2. It can be seen that the errors vary as the real ΔHbO_2^{br} changes and are also not simply proportional to the real ΔHbO_2^{br} , e.g. the errors are $\approx 9.8 \mu M$ for both real $\Delta HbO_2^{br} = 0 \mu M$ and real $\Delta HbO_2^{br} = 7 \mu M$ (circled in figure 2). This means that a simple percentage error defined as $(\text{predicted } \Delta HbO_2^{br} - \text{real } \Delta HbO_2^{br}) / \text{real } \Delta HbO_2^{br}$ will be very large for small real ΔHbO_2^{br} and in the case of real $\Delta HbO_2^{br} = 0 \mu M$ would be infinite. Instead, we have used the normalized RMS error defined below to assess the accuracy of the predictions collectively:

normalized RMS error

$$= \sqrt{\frac{\sum_{i=1}^P [\Delta HbO_{2, pd}^{br}(i) - \Delta HbO_2^{br}(i)]^2 + \sum_{i=1}^P [\Delta HHb_{pd}^{br}(i) - \Delta HHb^{br}(i)]^2}{\sum_{i=1}^P [\Delta HbO_2^{br}(i)]^2 + \sum_{i=1}^P [\Delta HHb^{br}(i)]^2}} \tag{10}$$

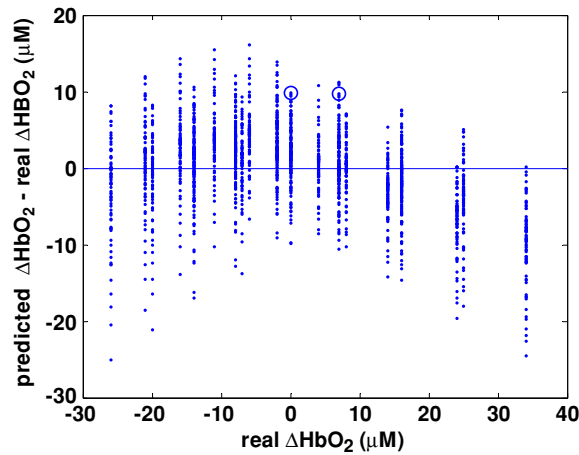


Figure 2. The errors between the predicted and real $\Delta\text{HbO}_2^{\text{br}}$ as a function of real $\Delta\text{HbO}_2^{\text{br}}$ based on a calibration with three detectors and mean time of flight data as shown in table 2(ii). The two circles correspond to errors $\approx 9.8 \mu\text{M}$ for both real $\Delta\text{HbO}_2 = 0 \mu\text{M}$ and $7 \mu\text{M}$.

where $\Delta\text{HbO}_2^{\text{br}}(i)/\Delta\text{HHb}^{\text{br}}(i)$ and $\Delta\text{HbO}_{2,\text{pd}}^{\text{br}}(i)/\Delta\text{HHb}_{\text{pd}}^{\text{br}}(i)$ are the real and predicted values of the i th realization (a particular combination of blood volume, SO_2 and extracerebral layer thickness in each layer) and P is the total number of realizations. The normalized RMS error can be interpreted as a fractional error with a value of 1 corresponding to an average error deviating by 100% from the real value and the minimum value of 0 representing total agreement. The advantage of using a fractional error term is that we can compare results obtained from using other ranges of real $\Delta\text{HbO}_2^{\text{br}}$ and $\Delta\text{HHb}^{\text{br}}$. The normalized RMS error is however a collective measure and is unable to indicate the specific error for a particular value of $\Delta\text{HbO}_2^{\text{br}}$ or $\Delta\text{HHb}^{\text{br}}$.

We are now ready to define the ‘nominal accuracy’ and ‘robustness’: nominal accuracy = $1 - \text{normalized RMS error resulting from using dataset (A)}$ and robustness = $1 - \text{normalized RMS error resulting from using dataset (B)}$. The ‘nominal accuracy’ and ‘robustness’ have a maximum value of 1 corresponding to total agreement between the real and predicted $\Delta\text{HbO}_2^{\text{br}}$ and $\Delta\text{HHb}^{\text{br}}$. A value of 0 corresponds to the average error deviating by 100% from the real value. The calculations of the nominal accuracy and the robustness defined here only differ by the input data being used. A high nominal accuracy corresponds to a good calibration for the prediction of $\Delta\text{HbO}_2^{\text{br}}$ and $\Delta\text{HHb}^{\text{br}}$ with the extracerebral layer thickness within the nominal range (defined as 9, 11 and 13 mm here), while a high robustness corresponds to a good calibration for the prediction of $\Delta\text{HbO}_2^{\text{br}}$ and $\Delta\text{HHb}^{\text{br}}$ with the extracerebral layer thickness varying over a wider range (defined as 7, 9, 11, 13 and 15 mm here).

3.4. The selection of the number of principal components

Before the calibrated PLS model can be used for predictions, the number of principal components (PCs) has to be specified first. The following describes the selection of the number of PCs. The RMS errors as a function of the number of PCs for the total number of detectors $M = 1, 2, 6$ and 10 are plotted in figure 3 where the measurement data $\Delta X_m = \Delta\tau_m$. The extracerebral layer thicknesses of 9, 11 and 13 mm have been included in the calibration. For clarity, only four curves are plotted here as an example. Since two $\Delta\tau_m$ (or ΔA_m) at two different wavelengths have been generated for each detector, there are $2 \times M$ measurement

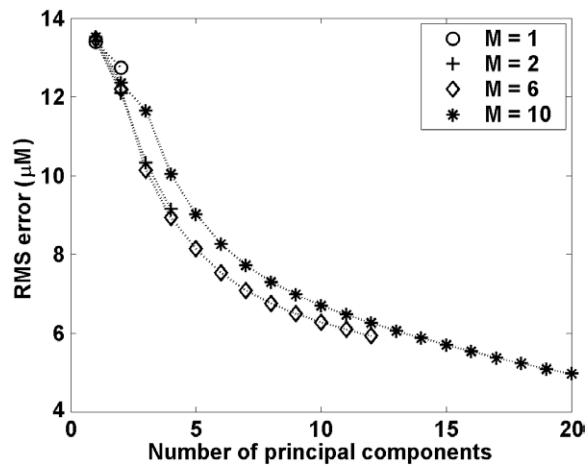


Figure 3. The RMS errors as a function of the number of PCs used: the mean times of flight have been used as the measurement data for the PLS calibration. Results are shown for the number of detectors, $M = 1, 2, 6$ and 10 .

values for one realization and thus the maximum number of PCs is also $2 \times M$. (When both ΔA_m and $\Delta \tau_m$ are used as measurement data, the maximum number of PC is $4 \times M$.) Each data point on figure 3 corresponds to the combination of detectors with the specified number of PCs which result in the least RMS error of all other possible combinations. As expected, as more PCs are used the RMS errors reduce but a point is soon reached when increasing the number of PCs does not lower the RMS error substantially, i.e. RMS error reduces by less than $0.5 \mu\text{M}$. The corresponding number of PCs is selected as our first criterion. For example, the number of PCs = 6 has been chosen for $M = 10$ in figure 3. It is generally desirable to use a smaller number of PCs because the resulting measurement weightings \mathbf{w} tend to be more robust to unknown measurement data. When all available PCs ($= 2 \times M$ or $4 \times M$) are used, the PLS calibration is essentially the same as multiple linear regression which is susceptible to collinearity and lacks robustness (Martens and Naes 1991). To avoid this, the maximum number of PCs selected is $(2 \times M) - 1$.

4. Results and discussion

4.1. The optimal number and locations of detectors

Using the criteria given in section 3.4, the number of PCs and the optimal combinations of detectors were found for detector numbers $M = 1-10$. As will be seen later, the improvement in estimation is small once $M > 3$, so data are only presented here for $M = 1, 2, 3, 6$ and 10 and the results are summarized in table 2. It contains the results obtained from three measurement datasets (i) $\Delta X_m = \Delta A_m$, (ii) $\Delta X_m = \Delta \tau_m$ and (iii) $\Delta X_m = [\Delta A_m \times \text{scaling factor } 1, \Delta \tau_m \times \text{scaling factor } 2]$. In dataset (iii), both ΔA_m and $\Delta \tau_m$ have been used together. The scaling factors are the inverse of standard deviations of the corresponding dataset and serve to normalize ΔA_m and $\Delta \tau_m$ so that their values are in the same range. As an example, figure 4 shows the measurement weightings, w_{m,HbO_2} (780 nm) of the optimal combinations of detectors as shown in table 2(ii). It can be seen that the measurement weightings are smooth or in other words do not oscillate between positive and negative which are signs of susceptibility in unknown datasets. The smoothness of the measurement weightings shown here are typical of a calibration performed with PLS and a small number of PCs. Although

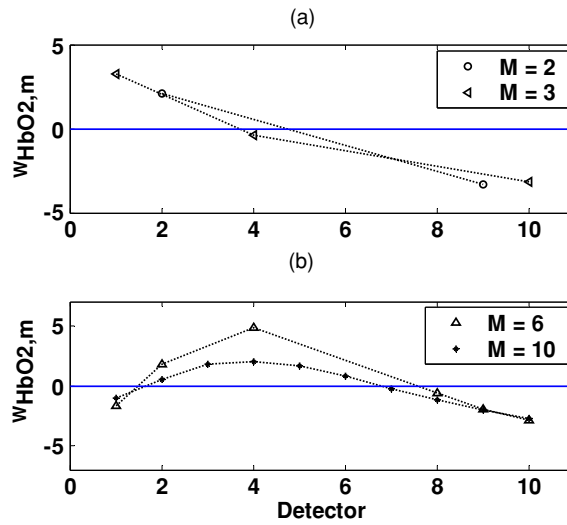


Figure 4. The measurement weightings, $w_{\text{HbO}_2,m}$ (780 nm) for the optimal combinations of detectors as shown in table 2(ii) using mean time of flight as the measurement data. Panel (a) the number of detectors, $M = 2$ and 3; (b) $M = 6$ and 10.

not shown here, the measurement weightings resulting from using datasets (i) and (iii) have similar smoothness.

Insights can be gained by investigating the measurement weightings shown in figure 4. For instance, the two detector case results in a positive weighting at detector 2 (10 mm source–detector spacing) and a negative weighting at detector 9 (45 mm spacing). It is known that a short spacing measurement is more sensitive to extracerebral absorption changes while a long spacing measurement is more sensitive to intracerebral absorption changes. The opposite signs indicate that certain subtraction of the extracerebral signal has been performed.

4.2. The nominal accuracy and robustness

Having obtained the optimal combinations of detectors and the number of PCs, we now use the nominal accuracy and robustness as defined in section 3.3 to compare the results. Figure 5 shows the nominal accuracy and robustness respectively resulting from using $M = 1, 2, 3, 6$ and 10. Table 2 shows that when $M = 1$ (a single detector system), the optimal location of the detector is at a source–detector spacing of 50 mm (detector 10) in all cases. At this spacing, photons measured have travelled deeper into the tissues. Yet, the nominal accuracy and robustness are close to zero for ΔA , corresponding to almost 100% deviation from the real values. This reflects a relatively high sensitivity of ΔA to changes in extracerebral absorption. Although the values are still low, the nominal accuracy and robustness of $\Delta \tau$ are approximately four times larger than those of ΔA , indicating a relatively higher intracerebral sensitivity. When both ΔA and $\Delta \tau$ are used together, even higher nominal accuracy and robustness are achieved. The availability of measurements with different depth sensitivities makes it more possible to subtract out the extracerebral absorption changes.

As M is increased to 2, the performance increases in all cases although that using both ΔA and $\Delta \tau$ together is still the best, followed by that using $\Delta \tau$ and then ΔA . When M is increased to 3 and beyond, the performances of all cases become comparable although using both measurements still often provides marginally better results.

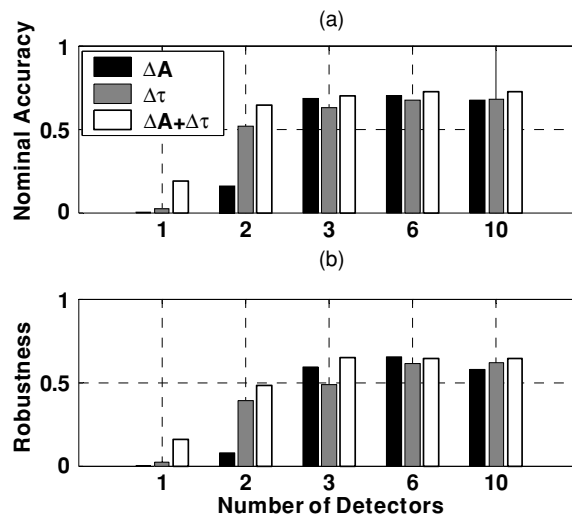


Figure 5. (a) Nominal accuracy and (b) robustness as the number of detectors increases (results are shown for $M = 1, 2, 6$ and 10). Three measurement datasets were used: (i) ΔA , (ii) $\Delta \tau$ and (iii) both ΔA and $\Delta \tau$ together.

5. Conclusions

Based on the PDP/MTSF frameworks, we have shown how the PLS can be exploited to calibrate for $\Delta \text{HbO}_2^{\text{br}}$ and $\Delta \text{HHb}^{\text{br}}$ over a range of blood volume, SO_2 and extracerebral layer thicknesses. The ‘nominal accuracy’ is used to assess the accuracy of estimating $\Delta \text{HbO}_2^{\text{br}}$ and $\Delta \text{HHb}^{\text{br}}$ within a nominal range of extracerebral layer thicknesses, while the ‘robustness’ indicates the accuracy of the estimation for extracerebral layer thicknesses that can extend beyond the nominal range used to derive the calibration. We have shown that PLS is a suitable calibration technique to obtain reasonably high nominal accuracy and robustness. By using a larger number of PCs in the PLS prediction, one can increase the nominal accuracy at the expense of robustness.

Our results show that in NIRS instruments using only one or two detectors, $\Delta \tau$ performs better than ΔA in terms of nominal accuracy and robustness, and the best performance was achieved when both $\Delta \tau$ and ΔA were used together. Our findings are consistent with the literatures which showed the depth sensitivity of $\Delta \tau$ to be higher than that of ΔA (Steinbrink *et al* 2001, Kohl-Baries *et al* 2002, Liebert *et al* 2004, 2005). An interesting extension of the current work would be to carry out PLS calibration using changes in the variance of the distribution of times of flight of photons which has been shown to have an even higher depth sensitivity than $\Delta \tau$ (Liebert *et al* 2004, 2005).

When three or more detectors are used, the performances of the three measurement datasets become comparable. This suggests that despite having a relatively low depth sensitivity, the performance of instruments that only measure ΔA can be compensated by using more detectors. This is a useful finding because continuous-wave systems used to make ΔA measurements are simpler and less expensive than the time or frequency-domain systems required for $\Delta \tau$ measurements.

We have not examined the performance of the other multi-layered methods as described in the introduction but we suspect that they may have robustness problem because most of these models were not designed to handle any uncertainty in the thicknesses of the layers. They also

often require computationally demanding Monte Carlo simulation for parameter estimation. Instead of relying on a physical model, the PLS calibrates itself based on the correlation between measurement and target data. One potential use for the technique discussed in this paper would be to use the PLS calibration to approximate the results for measurements on a particular multi-layered method over a range of different structural and physiological conditions. (Indeed, the PLS calibration presented here can be considered as the linear approximation of the photon transport software TOAST.) The measurement data in the PLS calibration would be the experimental measurements such as ΔA and/or $\Delta \tau$ and the target data would be the calculated results from the chosen multi-layered model such as $\Delta \mu_a$ or $\Delta \text{HbO}_2^{\text{br}} / \Delta \text{HHb}^{\text{br}}$ in the appropriate tissue component. The calibrated PLS model can then provide fast approximated results from new experimental measurements. This approach is expected to be most suited for linear models such as the PDP and MTSF based methods. Alternatively, one could perform a PLS calibration using ΔA and/or $\Delta \tau$ measured optically against $\Delta \text{HbO}_2^{\text{br}}$ and $\Delta \text{HHb}^{\text{br}}$ measured with other imaging techniques such as MRI/PET. The calibrated PLS model can potentially provide a linear approximation to the MRI/PET results using optical measurements.

The applicability of the results presented here relies on how accurately the measurement data (ΔA and $\Delta \tau$) are modelled. Since the photon transport modelling (the TOAST software package) used here is a simplification of the human head, the results given here are meant to be guidelines only. The aim of the paper is to outline the PLS method as a way to perform calibration with optical measurements. Several issues have not been considered in this study and can be investigated in the future. The cerebrospinal fluid (CSF), which acts as a light channel (Firbank *et al* 1996), has not been included in our head model. The boundaries of all layers are also assumed to be smooth which is far from the reality. The thickness of the grey matter has also not been altered. The CSF, uneven structures such as the sulci and variations in the thickness of the grey matter are all expected to change the light distribution (Okada *et al* 1995, Okada and Delpy 2003b). If these factors were included in the model, a similar analysis could be applied to determine the new optimal number, positions and measurement weightings of the detectors. The simulated data considered here were also noise free, although by limiting the furthest source–detector spacing to 50 mm we know from previous experimental evidence that a reasonable signal-to-noise ratio can be obtained with NIRS instrumentation at a sample rate of ≈ 1 Hz. The PLS calibration is less susceptible to low level noise and in such cases we would expect the results obtained here (measurement weightings, optimal number and positions of detectors) to be similar to those obtained if noise were included. With high levels of noise, however, one would expect the analysis performed here to work less favourably if detectors further away from the source were included in the determination of the optimal positions of detectors. The number of detectors required may also have to increase to compensate for uncertainties in the measurements.

Acknowledgments

The authors would like to thank Dr A Gibson, Dr J Riley and Professor S Arridge for their help in running the simulations and useful comments. This work was funded by the Wellcome Trust (GR 061558).

References

- Arridge S R, Schweiger M, Hiraoka M and Delpy D T 1993 A finite element approach for modeling photon transport in tissue *Med. Phys.* **20** 299–309

- Dayan I, Havlin S and Weiss G H 1992 Photon migration in a two-layer turbid medium: a diffusion analysis *J. Mod. Opt.* **39** 1567–82
- de Jong S 1993 An alternative approach to partial least squares regression *Chemometrics Intell. Lab. Syst.* **18** 251–63
- Delpy D T and Cope M 1997 Quantification in tissue near-infrared spectroscopy *Phil. Trans. R. Soc.* **352** 649–59
- Edwards A D, Richardson C, van der Zee P, Elwell C E, Wyatt J S, Cope M, Delpy D T and Reynolds E O R 1993 Measurement of haemoglobin flow and blood flow by near infrared spectroscopy *J. Appl. Physiol.* **75** 1884–9
- Elwell C E, Cope M, Edwards A D, Wyatt J S, Delpy D T and Reynolds E O R 1994 Quantification of adult cerebral hemodynamics by near-infrared spectroscopy *J. Appl. Physiol.* **77** 2753–60
- Essenpreis M, Elwell C E, van der Zee P, Arridge S R and Delpy D T 1993 Spectral dependence of temporal point spread functions in human tissues *Appl. Opt.* **32** 418–25
- Evans P D 1997 Non-invasive optical measurement of oxidative metabolism and haemoglobin parameters in tissue *PhD Thesis* (UK: University of Swansea)
- Fabbri F, Sassaroli A, Henry M E and Fantini S 2004 Optical measurements of absorption changes in two-layered diffusive media *Phys. Med. Biol.* **49** 1183–201
- Fantini S, Franceschini M A and Gratton E 1994 Semi-infinite geometry boundary problem for light migration in highly scattering media: a frequency-domain study in the diffusion approximation *J. Opt. Soc. Am.* **11** 2128–38
- Farrell T J, Patterson M S and Wilson B C 1992 A diffusion theory model of spatially resolved, steady state diffuse reflectance for the noninvasive determination of tissue optical properties *in vivo Med. Phys.* **19** 879–88
- Firbank M, Arridge S R, Schweiger M and Delpy D T 1996 An investigation of light transport through scattering bodies with non-scattering regions *Phys. Med. Biol.* **41** 767–83
- Gora F, Shinde S, Elwell C E, Goldstone J C, Cope M, Delpy D T and Smith M 2002 Non invasive measurement of cerebral blood flow in adults using near-infrared spectroscopy and indocyanine green: a pilot study *J. Neurosurg. Anesthesiol.* **14** 218–22
- Harris D N F, Cowans F M, Wertheim D A and Hamid S 1994 NIRS in adults—effects of increasing optode separation *Adv. Exp. Med. Biol.* **345** 837–40
- Hiraoka M, Firbank F, Essenpreis M, Cope M, Arridge S R, van der Zee P and Delpy D T 1993 A Monte Carlo investigation of optical pathlength in inhomogeneous tissue and its application to near-infrared spectroscopy *Phys. Med. Biol.* **38** 1859–76
- Hopton P, Walsh T S and Lee A 1999 Measurement of cerebral blood volume using near-infrared spectroscopy and indocyanine green elimination *J. Appl. Physiol.* **87** 1981–7
- Hueber D M, Franceschini M A, Ma H Y, Zhang Q, Ballesteros J R, Fantini S, Wallace D, Ntzachristos V and Chance B 2001 Non-invasive and quantitative near-infrared haemoglobin spectrometry in the piglet brain during hypoxic stress, using a frequency-domain multidistance instrument *Phys. Med. Biol.* **46** 41–62
- Hunter R J, Patterson M S, Farrell T J and Hayward J E 2002 Haemoglobin oxygenation of a two-layer tissue-simulating phantom from time-resolved reflectance: effect of top layer thickness *Phys. Med. Biol.* **47** 193–208
- Kienle A and Glanzmann T 1999 *In vivo* determination of the optical properties of muscle with time-resolved reflectance using a layered model *Phys. Med. Biol.* **44** 2689–702
- Kienle A and Patterson M S 1997 Improved solutions of the steady-state and time-resolved diffusion equations for reflectance from a semi-infinite turbid medium *J. Opt. Soc. Am.* **14** 246–54
- Kienle A, Patterson M S, Dgnitz N, Bays R, Wagnires G and van den Bergh H 1998 Noninvasive determination of the optical properties of two-layered turbid media *Appl. Opt.* **37** 779–91
- Kohl-Bareis M, Obrig H, Steinbrink J, Malak J, Uludag K and Villringer A 2002 Noninvasive monitoring of cerebral blood flow by a dye bolus method: separation of brain from skin and skull signals *J. Biomed. Opt.* **7** 464–70
- Leenders K L *et al* 1990 Cerebral blood flow, blood volume and oxygen utilization. Normal values and effect of age *Brain* **113** 27–47
- Leung T S, Elwell C E, Tachtsidis I, Henty J R and Delpy D T 2003 Measurement of the optical properties of the adult human head with spatially resolved spectroscopy and changes of posture *Adv. Exp. Med. Biol.* **540** 13–8
- Leung T S, Narendra A, Elwell C E, Delpy D T and Costeloe K 2004 A new method for the measurement of cerebral blood volume and total circulating blood volume using near infrared spatially resolved spectroscopy and indocyanine green: application and validation in neonates *Pediatr. Res.* **55** 134–41
- Liebert A, Wabnitz H, Steinbrink J, Möller M, Macdonald R, Rinneberg H, Villringer A and Obrig H 2005 Bed-side assessment of cerebral perfusion in stroke patients based on optical monitoring of a dye bolus by time-resolved diffuse reflectance *NeuroImage* **24** 426–35
- Liebert A, Wabnitz H, Steinbrink J, Obrig H, Möller M, Macdonald R, Villringer A and Rinneberg H 2004 Time-resolved multidistance near-infrared spectroscopy of the adult head: intracerebral and extracerebral absorption changes from moments of distribution of times of flight of photons *Appl. Opt.* **43** 3037–47
- Martens H and Naes T 1991 *Multivariate Calibration* (New York: Wiley)

- Matcher S J and Cooper C E 1994 Absolute quantification of deoxyhaemoglobin concentration in tissue near infrared spectroscopy *Phys. Med. Biol.* **39** 1295–312
- Matcher S J, Cope M and Delpy D T 1997 *In vivo* measurements of the wavelength dependence of tissue-scattering coefficients between 760 and 900 nm measured with time-resolved spectroscopy *Appl. Opt.* **36** 386–96
- Okada E and Delpy D T 2003a Near-infrared light propagation in an adult head model. II. Effect of superficial tissue thickness on the sensitivity of the near- infrared spectroscopy signal *Appl. Opt.* **42** 2915–21
- Okada E and Delpy D T 2003b Near-infrared light propagation in an adult head model. I. Modelling of low-level scattering in the cerebrospinal fluid layer *Appl. Opt.* **42** 2906–14
- Okada E, Firbank M, Schweiger M, Arridge S R, Cope M and Delpy D T 1995 A theoretical and experimental investigation of the effect of sulci on light propagation in brain tissue *Proc. SPIE* **2626** 2–8
- Schoberl J 2001 *NETGEN 4.0 User Manual* (Linz: Johannes Kepler University)
- Steinbrink J, Wabnitz H, Obrig H, Villringer A and Rinneberg H 2001 Determining changes in NIR absorption using a layered model of the human head *Phys. Med. Biol.* **46** 879–96
- Suzuki S, Takasaki S, Ozaki T and Kobayashi Y 1999 A tissue oxygenation monitor using NIR spatially resolved spectroscopy *Proc. SPIE* **3597** 582–92
- Wyatt J S, Cope M, Delpy D T, Richardson C E, Edwards A D, Wray S and Reynolds E O 1990 Quantitation of cerebral blood volume in human infants by near- infrared spectroscopy *J. Appl. Physiol.* **68** 1086–91